



Coherent control of ultrafast extreme ultraviolet transient absorption

Peng Peng^{1,2,3,4}✉, Yonghao Mi¹, Marianna Lytova², Mathew Britton², Xiaoyan Ding^{1,2},
A. Yu. Naumov¹, P. B. Corkum^{1,2} and D. M. Villeneuve^{1,2}✉

Ultrafast extreme ultraviolet (XUV) transient absorption is the process by which atoms and molecules absorb light on a timescale faster than the lifetime of the states involved. Coherent control uses quantum coherences to manipulate quantum pathways in light–matter interactions. Here we combine the two. We show that we can control the absorption spectral lineshape, changing it from Lorentzian to Fano to inverted Lorentzian and back again. The control is achieved by creating quantum coherence in the ground electronic state of hydrogen molecules, long before the arrival of the ultrafast XUV pulse. We show that the absorption can become negative at 12 eV, which is the optical gain. These observations provide new insights into the control of spectral lineshapes and open the way for achieving lasing without inversion in the XUV spectral range.

Coherent control in light–matter interactions has led to many exotic phenomena such as electromagnetically induced transparency^{1–3}, coherent population trapping^{4,5} and lasing without inversion (LWI)^{6–8}. These processes have been intensively investigated in recent years due to potential applications such as laser cooling⁹ and atomic clocks¹⁰. Recent advances in attosecond science have allowed us to extend coherent control to the extreme ultraviolet (XUV). Examples include the control of parity and direction of electrons emanating from the atom¹¹ and the hole density distribution in noble-gas ions¹².

The short duration and broad bandwidth of attosecond pulses are well suited for transient absorption measurements, leading to a new technique: attosecond transient absorption spectroscopy (ATAS)^{13–35}. ATAS experiments in atoms have been used to observe laser-controlled atomic absorption lineshapes^{17,18} and subcycle a.c. Stark shifts²⁰. Most of these experiments are performed when two pulses overlap in time, and therefore, the XUV pulse can be thought of as probing the dressed states of the atom produced by the near-infrared (NIR) pulse. This laser-controlled ATAS scheme has mostly been demonstrated in atoms, where the absorption spectrum is simple, and different transition lines are well separated in energy. However, it is more challenging in molecules, where the XUV pulse can excite numerous overlapping rovibronic transitions. The temporally overlapped or later-arrived NIR pulse can further broaden the absorption linewidth, ionize molecules or couple different states, resulting in a blurred or extremely complex absorption spectrum. On the other hand, an early arriving NIR pulse can produce quantum coherences in matter, which can last much longer than the NIR pulse duration. This field-free coherence is well suited for controlling electronic and nuclear dynamics. In the case of molecules, the later-arrived attosecond pulse excites electronic coherence in the system, leading to free induction decay (FID) that can last for picoseconds. The FID is modulated by the NIR-induced vibrational and rotational coherence. The complex coherent evolution of the system may change the spectral line profile and induce optical gain. Until now, a comprehensive study of such coherence effects in ATAS of molecules has been elusive.

Here we apply coherent control to ATAS. We use an NIR pulse to create rotational coherence in the ground electronic state of hydrogen (H₂) or deuterium (D₂) molecules. This superposition is probed with a broadband XUV pulse. We show that we can control the phase of the FID, leading to different absorption lineshapes. In the case of D₂, we achieve optical gain at 12 eV. This same approach can be applied to larger molecules, for example, polar molecules³⁶ or asymmetric top molecules³⁷.

Results

Schematic of pump–probe experiment. Figure 1a shows a schematic of our pump–probe experiment. In the pump step, an NIR pulse is used to create coherence ρ_{ab} between the rotational states $J=a$ and $J=b$ in the ground electronic state $X^1\Sigma_g^+$ of hydrogen or deuterium molecules (H₂: $a=1, b=3$; D₂: $a=0, b=2$). This superposition is probed with a time-delayed broadband XUV pulse, which simultaneously excites two dipole transitions. The upper state for these transitions is the rotational state $J'=c$ of the first electronic excited state $B^1\Sigma_u^+$ (H₂: $c=2$; D₂: $c=1$). Coherences between rotational eigenstates in a molecule lead to alignment of the molecular axes in space³⁸. In a classical picture, the molecules become kicked rotors after NIR excitation, which means that the angle between the molecular axis and polarization direction of the laser pulse changes over time, as shown in Fig. 1b. When the XUV pulse excites the rotational superposition, the coherence is transferred to the upper electronic state. The evolution of the coherence of all the three states will change the phase of FID $d(t)$. Figure 1c shows $d(t)$ for the $J=b \rightarrow J'=c$ transition at different molecular alignments. The absorption cross section is $\sigma(\omega) \approx \text{Im}[d(\omega)/E(\omega)]$, where $d(\omega)$ and $E(\omega)$ are connected to $d(t)$ and initial XUV pulse $E(t)$ via a Fourier transform¹⁷. Thus, the phase of $d(t)$ can be extracted from the absorption lineshape, as shown in Fig. 1d.

In the experiment, a 10 fs NIR pulse centred at 800 nm is focused into a pulsed gas jet of xenon. Through the process of high-harmonic generation, a series of attosecond pulses emanate from the gas jet covering the spectral range of 10–24 eV (refs. 29,39) (Methods provides more details). This emission is coherent and shorter than the

¹Joint Attosecond Science Laboratory, National Research Council and University of Ottawa, Ottawa, Ontario, Canada. ²Department of Physics, University of Ottawa, Ottawa, Ontario, Canada. ³School of Physical Science and Technology, ShanghaiTech University, Shanghai, China. ⁴Center for Transformative Science, ShanghaiTech University, Shanghai, China. ✉e-mail: pengpengnrc@gmail.com; David.Villeneuve@uottawa.ca

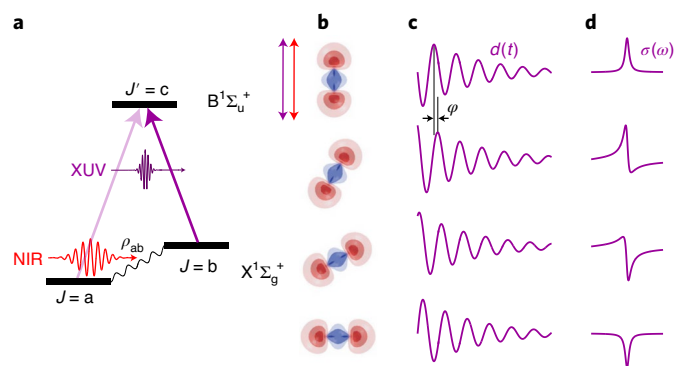


Fig. 1 | Absorption lineshape change induced by rotational coherence.

a, A Λ -type three-level system in H_2 or D_2 . The NIR pulse creates coherence ρ_{ab} between the rotational states $J = a$ and $J = b$ in the ground electronic state $X^1\Sigma_g^+$; then, a broadband XUV pulse excites two dipole transitions and transfers coherence to the upper state $J' = c$ of the first excited electronic state $B^1\Sigma_u^+$ (H_2 : $a=1, b=3, c=2$; D_2 : $a=0, b=2, c=1$).

b, Both XUV and NIR pulses are vertically polarized, the molecules become kicked rotors after NIR excitation, and the angle between the molecular axis and polarization changes over time. **c**, FID of the $J = b \rightarrow J' = c$ transition at different molecular alignments. For pure absorption (top), the induced dipole radiates out of phase with the incident attosecond pulse. **d**, Absorption lineshape $\sigma(\omega) \approx \text{Im}(d(\omega)/E(\omega))$ of the $J = b \rightarrow J' = c$ transition at different alignments. In the absence of coherence ρ_{abr} , the lineshape is always Lorentzian (top).

driving pulse, serving as the probe pulse. Meanwhile, a replica of the NIR pulse is picked off from the original pulse and used as the pump pulse to perform impulsive alignment of the molecules. The NIR pump pulse is combined with the XUV probe pulse and focused into a second pulsed gas jet containing either H_2 or D_2 . Both XUV and NIR pulses are vertically polarized, and their relative time delay is controlled by a delay stage. A high-resolution XUV spectrometer measures the spectrum of the XUV pulse after it passes through the second gas jet, with a spectral resolution of 12 meV at 12 eV.

XUV transient absorption in aligned H_2 . Figure 2a shows the static absorption of isotropic H_2 measured by blocking the NIR alignment pulse. The XUV pulse excites a vibrational series in the $\Delta J = J' - J = 0, \pm 1$ state. The positions of vibrational levels are indicated by grey vertical lines. There are several rotational transitions within one vibrational level (Supplementary Section 2). The rotational selection rule is

$$\Delta J = J' - J = 0, \pm 1,$$

where J' and J are the rotational quantum numbers of the upper and lower states, respectively. For the $B^1\Sigma_u^+$ state, ΔJ is forbidden. The positions of different rotational transition lines are labelled by shorter vertical lines. Figure 2b shows the transient absorption spectra OD. The modulation originates from the alignment-induced absorption lineshape change, as well as the absorption strength variation. The long delay of around 5.5 ps means the NIR pulse arrives much earlier than the XUV pulse, which is crucial for several reasons. First, it removes the influence of the subcycle a.c. Stark shifts of the NIR pulse¹⁷. Second, it avoids the broadening of the absorption linewidth by the NIR pulse¹⁸, which allows us to resolve the complex rovibronic transitions of H_2 . Third, it eliminates the multi-photon processes that are driven by a combination of the XUV pulse and NIR pulse^{21,23}. Figure 2e shows the Fourier transform of the experimental OD. The main beating frequency is 17.6 THz, corresponding to the energy difference between the $J = 1$

and $J = 3$ states⁴⁰ (Supplementary Section 3). Figure 2c,d shows the experimental and calculated differential absorption spectra ΔOD , respectively. The experimental and calculated results are in good agreement.

For a closer look at the coherence-induced absorption lineshape change, we enlarge a portion of Fig. 2a,b, as shown in Fig. 3a,b, respectively. The rotational transition $X(v=0, J=3)$ to $B(v'=5, J'=2)$ is labelled as P(3), whereas the transition $X(v=0, J=1)$ to $B(v'=5, J'=2)$ is labelled as R(1). For H_2 , the main rotational coherence is between $J=1$ and $J=3$, which is denoted as $\rho_{13} = |\rho_{13}|e^{i\Phi(\tau)}$, where $|\rho_{13}|$ is a constant amplitude; $\Phi(\tau) = (E_1 - E_3)\tau/\hbar$ is the delay-dependent phase; and E_1 and E_3 are the energies of the $J=1$ and $J=3$ states, respectively. Further, $\rho_{13}(\tau)$ oscillates as a function of delay τ and changes the phase of FID $d(t)$; therefore, the absorption lineshape periodically changes with the delay. As a result, the transition lines P(3) and R(1) are strongly modulated, as shown in Fig. 3b. There are other rotational transition lines that are partially overlapped with P(3) and R(1), but they are independent of time (Supplementary Sections 2 and 4). We use ΔOD to eliminate the time-independent absorption structures and isolate the lineshape change. The red curves in Fig. 3c show the experimental ΔOD lineshape of transition P(3) as it changes between a symmetric Lorentzian profile and an asymmetric Fano profile (we show transition P(3) as it is well separated from the other transitions in energy). The shaded regions represent the standard deviation of over 20 independent measurements.

The interconversion of Lorentzian and Fano lineshapes observed in our experiment is strongly connected to the previous demonstrations in helium¹⁷ due to the fact that the lineshape change in both works can be attributed to the control of the phase of the FID. In ref. ¹⁷, the NIR pulse overlaps or closely follows the XUV pulse, and the phase of the FID is controlled by the Stark effect of the NIR pulse. In our case, the NIR pulse arrives much earlier (~ 5.5 ps) than the XUV pulse, and the control of the phase of the FID is driven by the field-free rotational coherence. These two schemes can be complementary to each other. The laser-control scheme depends on the precise control of the NIR pulse intensity, which is efficient and well suited to atoms. Our scheme depends on the field-free quantum coherence, which is general in both atoms and molecules.

XUV transient absorption in aligned D_2 . The Λ -type three-level system (Fig. 1) shows that the absorption lineshape can be controlled by the quantum coherence. This is confirmed by our ATAS experiment in aligned H_2 . About three decades ago, a similar Λ -type three-level system was proposed for achieving LWI⁴¹. LWI has attracted substantial attention for its potential to produce laser light in the XUV range, which is difficult to achieve with conventional laser methods based on population inversion. Although various schemes in atomic vapours have been demonstrated^{6,7,42–45}, those studies involved continuous pumping and were limited to atoms and the visible spectral regime. The experimental verification of LWI in molecules and the XUV range remains elusive until now.

In the experiment with H_2 , the XUV pulse excites rotational superposition to the upper electronic state; therefore, it induces two coherent oscillating dipoles. The destructive interference between FID $d(t)$ instances is the basis of LWI⁶. However, we did not observe optical gain (negative OD) in Fig. 2b because the alignment excitation of H_2 is weak. As a result, we then turned to D_2 , which allows stronger alignment excitation for several reasons. First, the polarizability anisotropy of D_2 is larger than that of H_2 ; therefore, D_2 shows stronger alignment excitation under the same laser condition. Second, the rotational levels of D_2 are spaced closer in energy, which allows us to use a longer alignment pulse (50 fs) that contains more energy but has the same intensity. Third, D_2 and H_2 have different nuclear spin statistics and a lower rotational temperature can be used

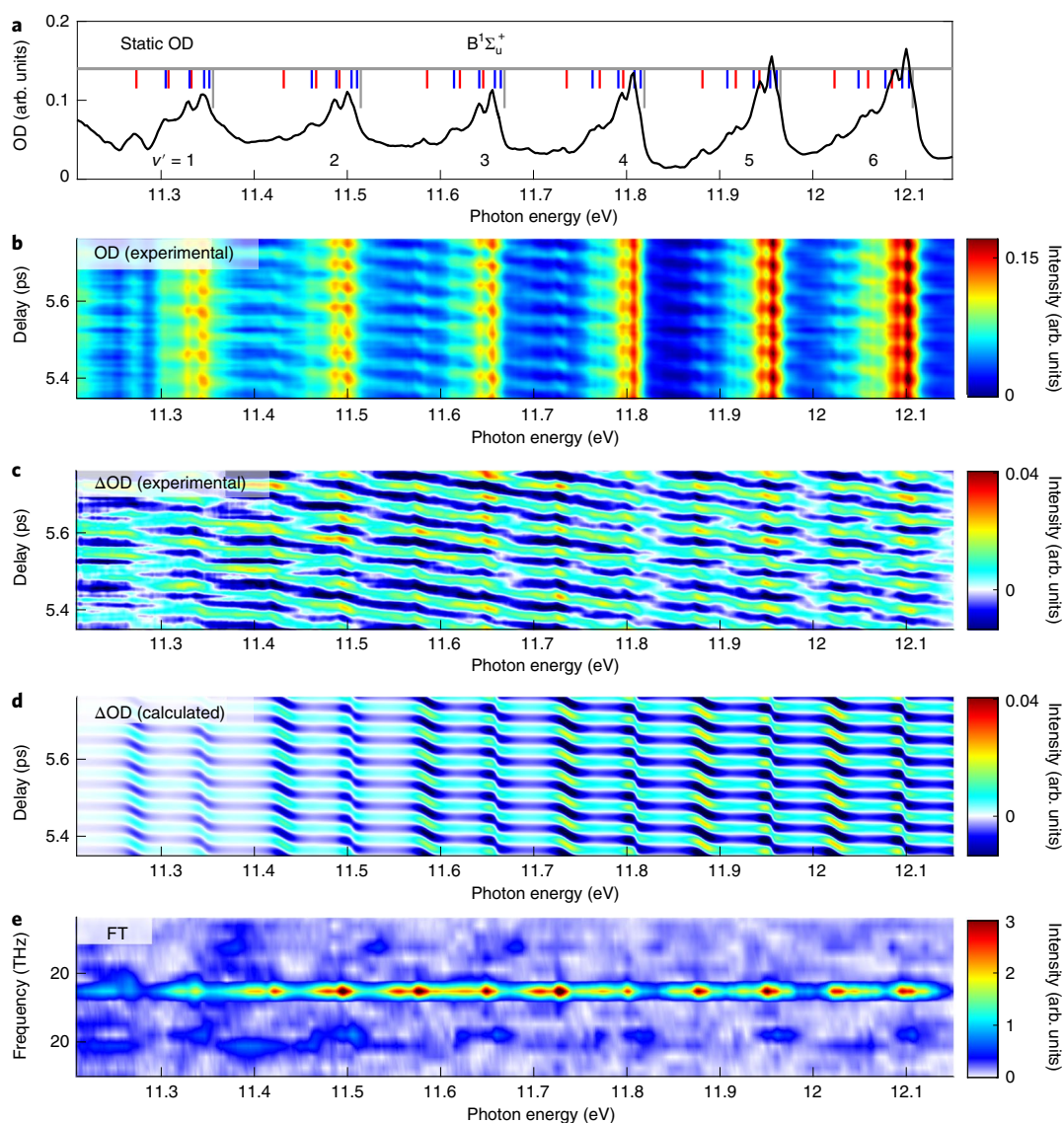


Fig. 2 | XUV transient absorption in aligned H_2 . **a**, Static absorption of isotropic H_2 molecules from 11.21 to 12.15 eV (black curve). The positions of vibrational levels of the $\text{B}^1\Sigma_u^+$ states are indicated by grey vertical lines. The positions of different rotational transition lines within the same vibrational state are labelled by shorter vertical lines: red (P branch; $\Delta J = -1$); blue (R branch; $\Delta J = 1$). **b**, Experimental transient absorption spectra OD; the XUV pulse follows the NIR pulse by a long delay of around 5.5 ps. The modulation originates from the alignment-induced absorption lineshape change, as well as the absorption strength variation. **c**, Experimental differential absorption spectra ΔOD . **d**, Calculated ΔOD . **e**, Fourier transform (FT) along the time delay axis of the experimental OD.

for D_2 to achieve dominant rotational coherence (Supplementary Section 3.1).

Figure 4a shows the static absorption of isotropic D_2 . The XUV pulse excites two vibrational series of $\text{B}^1\Sigma_u^+$ and $\text{C}^1\Pi_u$ states. Similarly, we use grey vertical lines to label the positions of vibrational levels. The positions of different rotational transition lines are labelled by shorter vertical lines. For D_2 , the rotational transition lines are spaced closer in energy due to a smaller rotational constant; the resolution of the spectrometer is not sufficient to resolve them. Figure 4b shows the transient absorption spectra OD. Like H_2 , the rotational coherence modifies the absorption lineshape. Negative OD (black spots) is observed for vibrational levels of the $\text{B}^1\Sigma_u^+$ state, but absent for vibrational levels of the $\text{C}^1\Pi_u$ state. The difference arises from the fact that the signals associated with parallel $X^1\Sigma_g^+ \rightarrow \text{B}^1\Sigma_u^+$ transition and perpendicular $X^1\Sigma_g^+ \rightarrow \text{C}^1\Pi_u$ transition have a different dependence on molecular alignment (Supplementary Section 5). Figure 4e shows the Fourier transform of the experimental OD. The main

beating frequency is 5.36 THz, corresponding to the energy difference between the $J=0$ and $J=2$ states. Figure 4c,d shows the experimental and calculated ΔOD values, respectively.

For a closer look at the coherence-induced optical gain, we enlarge a portion of Fig. 4b, as shown in Fig. 5a. Figure 5b shows the lineouts of OD at three different delays. The lineshape changes from an asymmetric Fano profile (red line; Fano parameter $q \approx 0.58$) to a symmetric Lorentzian profile (black line; $q \rightarrow \infty$), and then to a Fano profile with a negative q parameter (blue line; $q \approx -1.73$). The black spots in Fig. 5a and red line in Fig. 5b show the optical gain at 12.4 eV. Due to the high nonlinearity of high-harmonic generation, the stability of XUV light is $\sim 3.7\%$ in our experiment; light fluctuation can also randomly cause negative OD. To confirm the optical gain, we performed 20 independent measurements, and the standard deviation is shown as the shaded regions in Fig. 5b. Although the gain is weak, it is repeatable. Furthermore, the negative OD appears with a period of 180 fs, as shown in Fig. 5a. This period

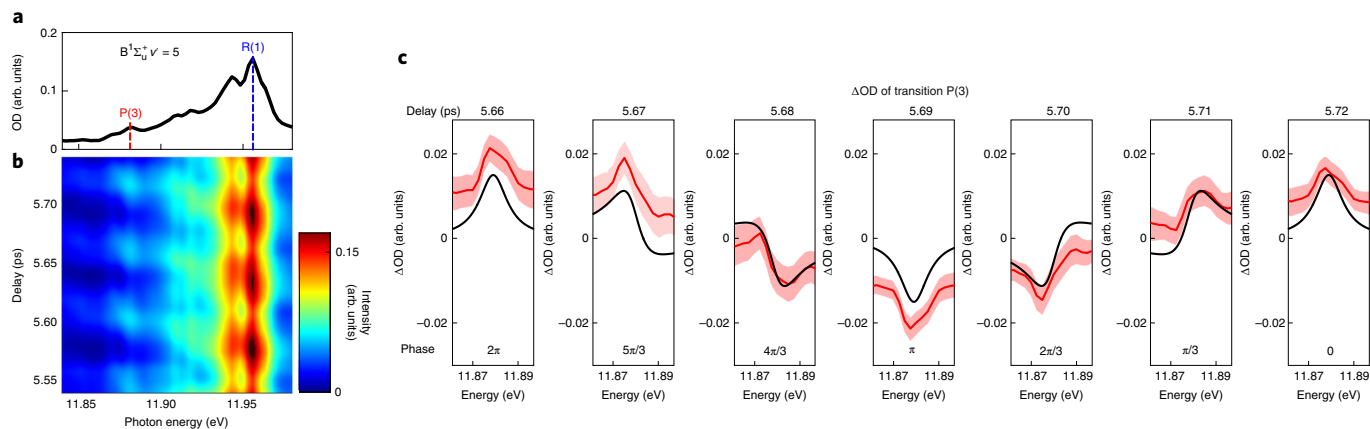


Fig. 3 | Absorption lineshape of an individual rotational transition in aligned H_2 . **a**, Zoomed-in view of Fig. 2a; the photon energy range covers the excitations from $v=0$ of $X^1\Sigma_g^+$ to $v'=5$ of the $B^1\Sigma_u^+$ state. Due to the high spectral resolution (12 meV), the rotational transition lines can be partially resolved. P(3): rotational transition from $X(v=0, J=3)$ to $B(v'=5, J'=2)$; R(1): rotational transition from $X(v=0, J=1)$ to $B(v'=5, J'=2)$. **b**, Zoomed-in view of Fig. 2b; OD versus time delay. **c**, Lineouts of experimental ΔOD (red curves) and calculated ΔOD (black curves) of transition P(3). The shaded regions represent the standard deviation of over 20 independent measurements.

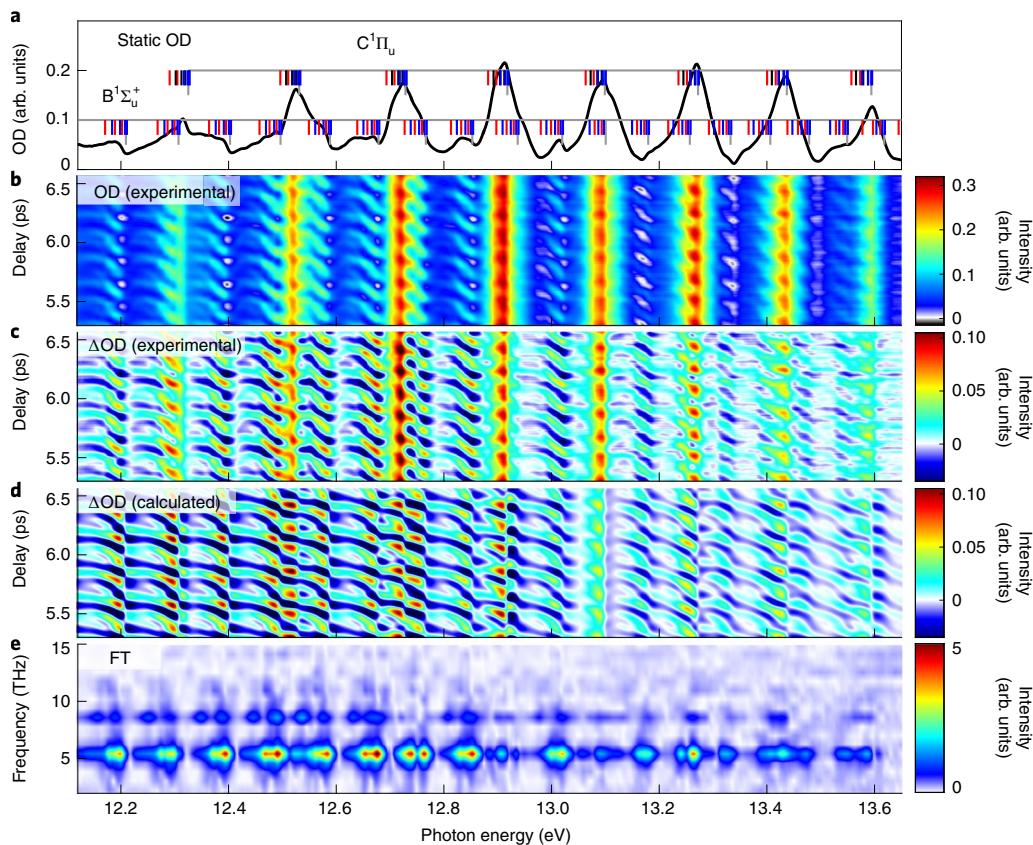


Fig. 4 | XUV transient absorption in aligned D_2 . **a**, Static absorption of isotropic D_2 molecules from 12.1 to 13.6 eV (black curve). The positions of vibrational levels of the $B^1\Sigma_u^+$ and $C^1\Pi_u$ states are indicated by the grey vertical lines. The positions of different rotational transition lines within the same vibrational state are labelled by shorter vertical lines: red (P branch; $\Delta J=-1$); blue (R branch; $\Delta J=1$); black (Q branch; $\Delta J=0$). **b**, Experimental transient absorption spectra OD. The XUV pulse follows the NIR pulse by a long delay of around 6 ps. The modulation originates from the alignment-induced absorption lineshape change. **c**, Experimental differential absorption spectra ΔOD . **d**, Calculated ΔOD . **e**, Fourier transform of the experimental OD.

corresponds to the energy difference between the rotational states $J=0$ and $J=2$ of the ground electronic state of D_2 , which further confirms that the negative OD is not caused by random fluctuation; instead, it arises from the quantum coherence evolution.

There is no population inversion in our experiment for several reasons. First, in the pump step, the upper electronic state is unpopulated as the NIR pulse frequency is far away from resonance. Second, in the probe step, the attosecond pulse is very weak,

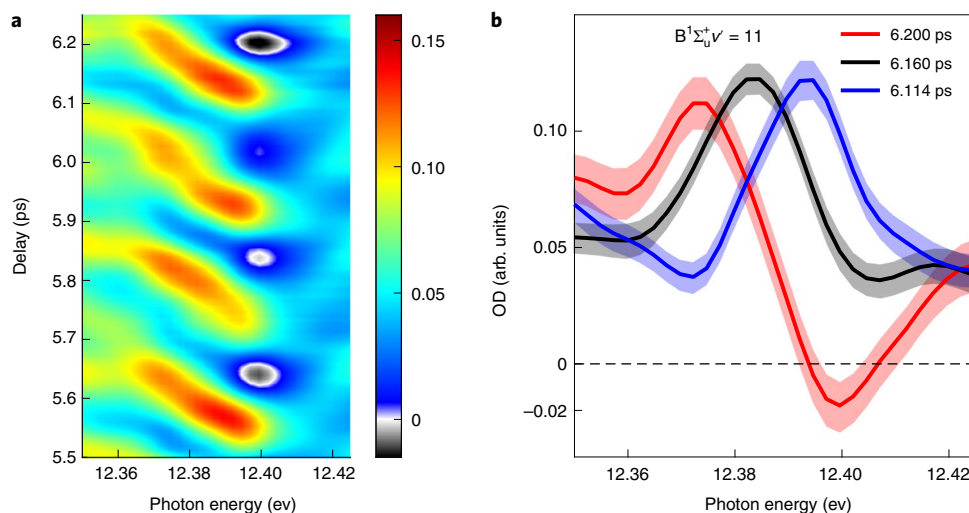


Fig. 5 | Optical gain in aligned D_2 . **a**, Zoomed-in view of Fig. 4b; the photon energy range covers the excitations from $v=0$ of $X^1\Sigma_g^+$ to $v'=11$ of the $B^1\Sigma_u^+$ state. The black regions demonstrate negative OD. **b**, Lineouts of OD at three different pump-probe delays. The shaded regions represent the standard deviation over 20 independent measurements. The OD at 12.4 eV for 6.2 ps is negative, that is, optical gain is achieved.

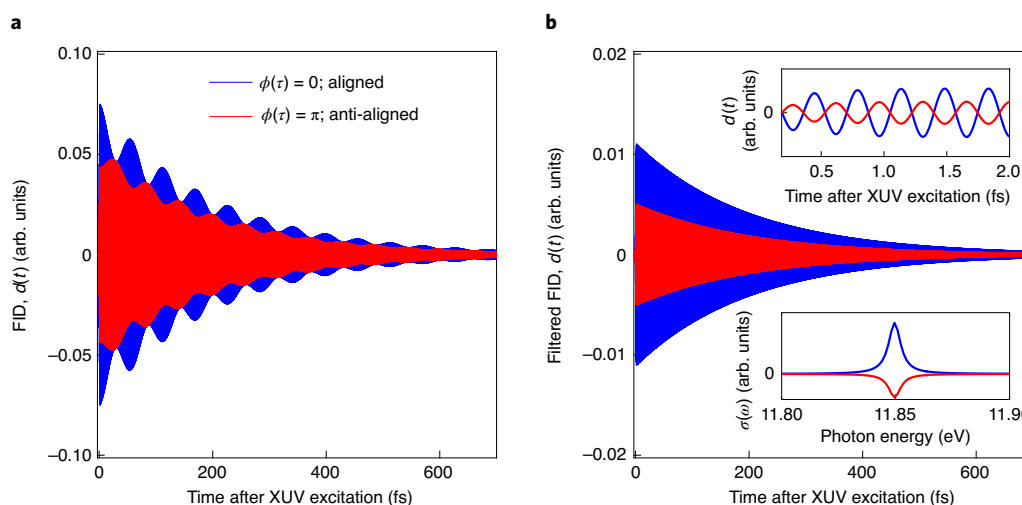


Fig. 6 | Calculated FID of a three-level system based on H_2 . **a**, FID $d(t)$ for aligned (blue curve) and anti-aligned (red curve) H_2 . A larger FID leads to greater absorption. **b**, Filtered $d(t)$ for the $J=3 \rightarrow J'=2$ transition. The top inset shows a magnification of filtered $d(t)$, which shows different amplitudes and phases. The bottom inset shows the corresponding absorption cross section $\sigma(\omega)$, showing different lineshapes (positive Lorentzian and negative Lorentzian).

and very little population is transferred to the upper state. Third, the NIR pulse arrives much earlier (~ 6 ps) than the attosecond pulse, which removes the influence of multi-photon processes^{21,23}. Thus, the observation of optical gain at 12.4 eV may encourage the extension of the LWI idea from the visible^{6,7,42–45} to the XUV spectral regime.

Discussion

To understand the absorption lineshape change and optical gain induced by rotational coherence, we develop a full quantum model. More details are provided in Supplementary Section 3. The rotational coherences and populations of the lower states are calculated by using a density matrix approach⁴⁶. We consider the upper states to be different vibrational progressions of different electronic states and calculate all the rotational transitions. The model results are shown in Fig. 2d for H_2 and Fig. 4d for D_2 . Here we illustrate the calculation using a simplified three-level system based on H_2 (Methods

provides more details). We label the states as ‘1’ for $X(v=0, J=1)$, ‘3’ for $X(v=0, J=3)$ and ‘2’ for $B(v'=5, J'=2)$, with populations ρ_{11} , ρ_{33} and ρ_{22} , respectively. The rotational coherence of the two lower states is $\rho_{13} = |\rho_{13}|e^{i\Phi(\tau)}$, where $|\rho_{13}|$ is the coherence amplitude, which is a constant after NIR pulse excitation, and $\Phi(\tau) = (E_1 - E_3)\tau/\hbar$ is the delay-dependent coherence phase; $E_1 - E_3$ is the energy difference between the two lower states and τ is the delay between the NIR and XUV pulse.

By solving the Liouville–von Neumann equation of the three-level system, we calculated the FID signal, as shown in Fig. 6a. Probe times τ for the aligned (Fig. 6a, blue curve; coherence phase, $\Phi(\tau)=0$) and anti-aligned (Fig. 6a, red curve; coherence phase, $\Phi(\tau)=\pi$) cases are shown. Low-frequency modulations are induced by coherence between the different rotational states. High-frequency oscillations are mainly determined by the electronic transition frequency (~ 12 eV in this calculation, and not visible on this timescale). The high-frequency oscillations

consist of two frequencies, corresponding to the $J = 1 \rightarrow J' = 2$ and $J = 3 \rightarrow J' = 2$ transitions. By applying a Fourier filter, we extract the FID for the $J = 3 \rightarrow J' = 2$ transition, as shown in Fig. 6b. The top inset of Fig. 6b is a magnification of the main figure, which clearly shows different amplitudes and phases. The bottom inset of Fig. 6b is the corresponding absorption cross section $\sigma(\omega) \approx \text{Im}(d(\omega)/E(\omega))$. Here $\sigma(\omega)$ shows the different lineshapes, which agrees with our experimental result (Fig. 3c; delays of 5.72 and 5.69 ps).

Mathematically, the transient absorption cross section for the $J = 3 \rightarrow J' = 2$ transition is

$$\sigma_{32}(\omega, \tau) = \frac{4\pi\omega}{c} \left[\rho_{33} |d_{32}|^2 \frac{\frac{\Gamma}{2}}{(\omega - \omega_{32})^2 + \frac{\Gamma^2}{4}} + |d_{32}d_{21}\rho_{31}| \frac{\frac{\Gamma}{2} \cos[\phi(\tau)] + (\omega - \omega_{32}) \sin[\phi(\tau)]}{(\omega - \omega_{32})^2 + \frac{\Gamma^2}{4}} \right], \quad (1)$$

where d represents the transition dipole moment; $\omega_{32} = (E_2 - E_3)/\hbar$; E_2 and E_3 are the energies of the upper and lower states, respectively; and Γ is the decay rate of the upper state. The first term in equation (1) describes a time-independent Lorentzian lineshape that is always positive, whereas the second term contains both absorptive and dispersive parts that can be positive or negative. The relative weights between these two terms are roughly determined by ρ_{33} and $|\rho_{31}|$. For H_2 , the alignment excitation is weak, so the second term is small. We calculated ΔOD using equation (1), as shown by the black curves in Fig. 3c. Phase $\phi(\tau)$ for the $J = 3 \rightarrow J' = 2$ transition was extracted by analysing the lineshape, as shown in Fig. 3c, bottom. Also, D_2 is easier to align than H_2 , which means a larger second term in equation (1). This allows optical gain to be achieved.

In conclusion, we have demonstrated the coherent control of the absorption lineshape using rotational wave packets in H_2 . By tracing the lineshape change for individual rotational transitions, we extracted the phase of the dipole response function from the lineshape analysis. This mechanism was further investigated in D_2 gas, where we achieved an optical gain at 12 eV without population inversion. Distinct from previous demonstrations of LWI in the visible spectral regime^{6,7,42–45}, the optical gain is driven by lineshape change caused by rotational coherence in the ground state.

Our study provides a benchmark for the coherence-induced lineshape change and optical gain. This mechanism may widely exist in molecular systems, from rotational and vibrational wave packets to electron excitations. For example, in the N_2^+ air laser, where the gain mechanism is not fully understood^{47–49}, the coherence-induced lineshape change may help solve these puzzles. In addition, the extracted dipole response phase will give a further insight into the dynamics of quantum coherence, which is important for understanding Fano resonances and ultrafast charge migration^{17,36}. Looking forward, future experiments applying a water-window high-harmonic source or a short-pulse X-ray free-electron laser could excite core-level electrons^{24,26}, potentially extending the optical gain frequency to the X-ray regime. More complex molecules can be controlled by a two-colour laser field or pulse sequence^{36,37}, permitting similar studies to be applied to polar molecules or asymmetric top molecules.

Online content

Any methods, additional references, Nature Research reporting summaries, source data, extended data, supplementary information, acknowledgements, peer review information; details of author contributions and competing interests; and statements of data and code availability are available at <https://doi.org/10.1038/s41566-021-00907-7>.

Received: 15 March 2021; Accepted: 8 October 2021;
Published online: 13 December 2021

References

- Safavi-Naeini, A. H. et al. Electromagnetically induced transparency and slow light with optomechanics. *Nature* **472**, 69–73 (2011).
- Fleischhauer, M., Imamoglu, A. & Marangos, J. P. Electromagnetically induced transparency: optics in coherent media. *Rev. Mod. Phys.* **77**, 633–673 (2005).
- Wang, C. Q. et al. Electromagnetically induced transparency at a chiral exceptional point. *Nat. Phys.* **16**, 334–340 (2020).
- Arimondo, E. Coherent population trapping in laser spectroscopy. *Prog. Opt.* **35**, 257–354 (1996).
- Donarini, A. et al. Coherent population trapping by dark state formation in a carbon nanotube quantum dot. *Nat. Commun.* **10**, 381 (2019).
- Scully, M. O. & Fleischhauer, M. Lasers without inversion. *Science* **263**, 337–338 (1994).
- Mompart, J. & Corbalán, R. Lasing without inversion. *J. Opt. B: Quantum Semiclass. Opt.* **2**, R7–R24 (2000).
- Richter, M. et al. Rotational quantum beat lasing without inversion. *Optica* **7**, 586–592 (2020).
- Langin, T. K., Gorman, G. M. & Killian, T. C. Laser cooling of ions in a neutral plasma. *Science* **363**, 61–64 (2019).
- Ludlow, A. D., Boyd, M. M., Ye, J., Peik, E. & Schmidt, P. O. Optical atomic clocks. *Rev. Mod. Phys.* **87**, 637–701 (2015).
- Villeneuve, D. M., Hockett, P., Vrakking, M. J. J. & Niikura, H. Coherent imaging of an attosecond electron wave packet. *Science* **356**, 1150–1153 (2017).
- Goulielmakis, E. et al. Real-time observation of valence electron motion. *Nature* **466**, 739–743 (2010).
- Hosler, E. R. & Leone, S. R. Characterization of vibrational wave packets by core-level high-harmonic transient absorption spectroscopy. *Phys. Rev. A* **88**, 023420 (2013).
- Wei, Z. R. et al. Elucidating the origins of multimode vibrational coherences of polyatomic molecules induced by intense laser fields. *Nat. Commun.* **8**, 735 (2017).
- Wu, M., Chen, S., Camp, S., Schafer, K. J. & Gaarde, M. B. Theory of strong-field attosecond transient absorption. *J. Phys. B: At. Mol. Opt. Phys.* **49**, 062003 (2016).
- Santra, R., Yakovlev, V. S., Pfeifer, T. & Loh, Z.-H. Theory of attosecond transient absorption spectroscopy of strong-field-generated ions. *Phys. Rev. A* **83**, 033405 (2011).
- Ott, C. et al. Lorentz meets Fano in spectral line shapes: a universal phase and its laser control. *Science* **340**, 716–720 (2013).
- Kaldun, A. et al. Observing the ultrafast buildup of a Fano resonance in the time domain. *Science* **354**, 738–741 (2016).
- Bengtsson, S. et al. Space-time control of free induction decay in the extreme ultraviolet. *Nat. Photon.* **11**, 252–258 (2017).
- Chini, M. et al. Subcycle a.c. Stark shift of helium excited states probed with isolated attosecond pulses. *Phys. Rev. Lett.* **109**, 073601 (2012).
- Chini, M. et al. Sub-cycle oscillations in virtual states brought to light. *Sci. Rep.* **3**, 1105 (2013).
- Liao, C.-T., Sandhu, A., Camp, S., Schafer, K. J. & Gaarde, M. B. Beyond the single-atom response in absorption line shapes: probing a dense, laser-dressed helium gas with attosecond pulse trains. *Phys. Rev. Lett.* **114**, 143002 (2015).
- Drescher, L. et al. Extreme-ultraviolet spectral compression by four-wave mixing. *Nat. Photon.* **15**, 263–266 (2021).
- Pertot, Y. et al. Time-resolved X-ray absorption spectroscopy with a water window high-harmonic source. *Science* **355**, 266–267 (2017).
- Kobayashi, Y., Chang, K. F., Zeng, T., Neumark, D. M. & Leone, S. R. Direct mapping of curve-crossing dynamics in IBR by attosecond transient absorption spectroscopy. *Science* **365**, 79–83 (2019).
- Loh, Z.-H. et al. Observation of the fastest chemical processes in the radiolysis of water. *Science* **367**, 179–182 (2020).
- Reduzzi, M. et al. Observation of autoionization dynamics and sub-cycle quantum beating in electronic molecular wave packets. *J. Phys. B: At. Mol. Opt. Phys.* **49**, 065102 (2016).
- Cheng, Y. et al. Reconstruction of an excited-state molecular wave packet with attosecond transient absorption spectroscopy. *Phys. Rev. A* **94**, 023403 (2016).
- Peng, P. et al. Symmetry of molecular Rydberg states revealed by XUV transient absorption spectroscopy. *Nat. Commun.* **10**, 5269 (2019).
- Schultze, M. et al. Attosecond band-gap dynamics in silicon. *Science* **346**, 1348–1352 (2014).
- Lucchini, M. et al. Attosecond dynamical Franz-Keldysh effect in polycrystalline diamond. *Science* **353**, 916–919 (2016).
- Moulet, A. et al. Soft X-ray excitonics. *Science* **357**, 1134–1138 (2017).
- Schlaepfer, F. et al. Attosecond optical-field-enhanced carrier injection into the GaAs conduction band. *Nat. Phys.* **14**, 560–564 (2018).
- Warrick, E. R. et al. Attosecond transient absorption spectroscopy of molecular nitrogen: vibrational coherences in the $b^1\Sigma_u^+$ state. *Chem. Phys. Lett.* **683**, 408–415 (2017).

35. Drescher, L. et al. State-resolved probing of attosecond timescale molecular dipoles. *J. Phys. Chem. Lett.* **10**, 265–269 (2019).
36. Kraus, P. M. et al. Measurement and laser control of attosecond charge migration in ionized iodoacetylene. *Science* **350**, 790–795 (2015).
37. Lee, K. F., Villeneuve, D. M., Corkum, P. B., Stolow, A. & Underwood, J. G. Field-free three-dimensional alignment of polyatomic molecules. *Phys. Rev. Lett.* **97**, 173001 (2006).
38. Stapelfeldt, H. & Seideman, T. Colloquium: aligning molecules with strong laser pulses. *Rev. Mod. Phys.* **75**, 543–557 (2003).
39. Hammond, T. J. et al. Integrating solids and gases for attosecond pulse generation. *Nat. Photon.* **11**, 594–599 (2017).
40. Mi, Y. H. et al. Clocking enhanced ionization of hydrogen molecules with rotational wave packets. *Phys. Rev. Lett.* **125**, 173201 (2020).
41. Scully, M. O., Zhu, S.-Y. & Gavrielides, A. Degenerate quantum-beat laser: lasing without inversion and inversion without lasing. *Phys. Rev. Lett.* **62**, 2813–2816 (1989).
42. Harris, S. E. Lasers without inversion: interference of lifetime-broadened resonances. *Phys. Rev. Lett.* **62**, 1033–1036 (1989).
43. Fry, E. S. et al. Atomic coherence effects within the sodium D1 line: lasing without inversion via population trapping. *Phys. Rev. Lett.* **70**, 3235–3238 (1993).
44. van der Veer, W. E., van Diest, R. J. J., Dönszelmann, A. & van Linden van den Heuvell, H. B. Experimental demonstration of light amplification without population inversion. *Phys. Rev. Lett.* **70**, 3243–3246 (1993).
45. Nottelmann, A., Peters, C. & Lange, W. Inversionless amplification of picosecond pulses due to Zeeman coherence. *Phys. Rev. Lett.* **70**, 1783–1786 (1993).
46. Ramakrishna, S. & Seideman, T. Dissipative dynamics of laser induced nonadiabatic molecular alignment. *J. Chem. Phys.* **124**, 034101 (2006).
47. Yao, J. P. et al. High-brightness switchable multiwavelength remote laser in air. *Phys. Rev. A* **84**, 051802 (2011).
48. Xu, H. L., Lötstedt, E., Iwasaki, A. & Yamanouchi, K. Sub-10-fs population inversion in N_2^+ in air lasing through multiple state coupling. *Nat. Commun.* **6**, 8347 (2015).
49. Britton, M. et al. Testing the role of recollision in N_2^+ air lasing. *Phys. Rev. Lett.* **120**, 133208 (2018).

Publisher's note Springer Nature remains neutral with regard to jurisdictional claims in published maps and institutional affiliations.

© The Author(s), under exclusive licence to Springer Nature Limited 2021

Methods

Experimental setup. In the experiment, NIR laser pulses were generated by a Ti:sapphire laser system (100 Hz; 14 mJ; 800 nm; 50 fs). Approximately 1.6 mJ was sent into a differentially pumped hollow-core fibre (inner diameter, 250 μm) filled with 0.7 bar of argon to create a 10 fs pulse centred at around 800 nm. This pulse was focused into a pulsed gas jet of xenon (3 bar backing pressure and 250 μm nozzle), where high-harmonic generation took place. A thin ($80 \pm 10 \mu\text{m}$) monocrystalline quartz plate was placed approximately 2 cm before the xenon gas jet to broaden the spectrum through self-phase modulation and to create some second harmonics of 800 nm (refs. ^{29,39}). The intensity at the quartz plate was $3 \times 10^{13} \text{ W cm}^{-2}$, which was below the damage threshold ($< 4 \times 10^{13} \text{ W cm}^{-2}$), but strong enough to generate new spectral components through self-phase modulation. The bandwidth of each harmonic increased from 0.7 to 2.3 eV, and the total spectrum spanned 10–24 eV (ref. ²⁹). The residual NIR driving field was eliminated by a 500- μm -diameter pinhole and two silicon mirrors. A replica of the 10 fs NIR pulse was used as the pump pulse to perform impulsive alignment of the H_2 molecules (a large rotational energy spacing requires a broadband alignment pulse). For D_2 molecules, the alignment pulse was a 50 fs NIR pulse picked off from the original pulse to achieve a higher alignment degree. The NIR pump pulse was combined with the XUV probe pulse with a holey mirror. The XUV and NIR pulses propagated non-collinearly and intersected at the absorption gas jet (250 μm nozzle; gas density, $\sim 10^{17} \text{ cm}^{-3}$; interaction length, $\sim 0.5 \text{ mm}$) with a crossing angle of 18 mrad. The transmitted XUV spectrum was dispersed in a flat-field XUV spectrometer and detected by a microchannel plate detector. The XUV spectrometer was set at around 12 eV to achieve a high spectral resolution of 12 meV. Further details of the experimental setup are provided in Supplementary Section 1 and Supplementary Fig. 1.

Simplified three-level system. To clarify the FID in the coherently excited molecules, we model H_2 as a simplified three-level system. The states are labelled as ‘1’ for $X(v=0, J=1)$, ‘3’ for $X(v=0, J=3)$ and ‘2’ for $B(v'=5, J'=2)$. The evolution of the three-level system is described by the following Liouville–von Neumann equation:

$$\frac{d\rho(t)}{dt} = -\frac{i}{\hbar} [H, \rho(t)], \quad (2)$$

and the Hamiltonian H and density operator ρ are given as

$$H = \begin{bmatrix} E_2 & -\mu_{32}E_{\text{XUV}}(t) & -\mu_{12}E_{\text{XUV}}(t) \\ -\mu_{32}E_{\text{XUV}}(t) & E_3 & 0 \\ -\mu_{12}E_{\text{XUV}}(t) & 0 & E_1 \end{bmatrix}; \quad (3)$$

$$\rho = \begin{bmatrix} \rho_{22} & \rho_{23} & \rho_{21} \\ \rho_{32} & \rho_{33} & \rho_{31} \\ \rho_{12} & \rho_{13} & \rho_{11} \end{bmatrix},$$

where μ_{32} and μ_{12} are the transition matrix elements; $E_{\text{XUV}}(t)$ is the XUV field; E_1 , E_2 and E_3 are the energies and ρ_{11} , ρ_{22} and ρ_{33} are the populations of the three levels;

the off-diagonal elements of ρ denote quantum coherence between the different levels. The initial density matrix elements can be achieved by calculating the molecular alignment, as shown in Supplementary Section 3.1. Then, we solve the Liouville equation by the Crank–Nicolson method and find the time-dependent density matrix ρ . The FID is $d(t) = \text{Tr}(\mu\rho) = 2\text{Re}(\mu_{12}\rho_{12} + \mu_{32}\rho_{32})$. Figure 6 shows the calculated $d(t)$, which has both low-frequency modulations (induced by coherence between the different rotational states) and high-frequency oscillations (mainly determined by the electronic transition frequency). For different times of molecular alignments, $d(t)$ will have different amplitudes and phases, which leads to different absorption strengths and lineshapes.

Data availability

The data that support the findings of this study are available from the corresponding authors upon reasonable request.

Code availability

The code used in this study is available from the corresponding authors upon reasonable request.

Acknowledgements

We thank D. Crane and R. Kroeker for technical support. We acknowledge fruitful discussions with A. Korobenko, G. Xin, A. Stolow, M. Spanner, B. Bernhardt and V. Schuster. This research is supported by the NSERC Discovery Grant program (RGPIN-327147-2012; D.M.V.), and by the US Army Research Office through award W911NF-14-1-0383 (D.M.V.). We acknowledge support of the Joint Centre for Extreme Photonics (P.B.C. and D.M.V.), the DFG (grant no. MI 2434/1-1; Y.M.), and the start-up grant of ShanghaiTech University (P.P.).

Author contributions

P.P. and D.M.V. conceived and planned the experiment. P.P., Y.M. and X.D. conducted the measurements. P.P. and D.M.V. analysed and interpreted the data. M.L. and M.B. provided the theoretical supporting calculations. A.Y.N., P.B.C. and D.M.V. supervised the project. P.P. wrote the manuscript, with inputs from all the authors.

Competing interests

The authors declare no competing interests.

Additional information

Supplementary information The online version contains supplementary material available at <https://doi.org/10.1038/s41566-021-00907-7>.

Correspondence and requests for materials should be addressed to Peng Peng or D. M. Villeneuve.

Peer review information *Nature Photonics* thanks the anonymous reviewers for their contribution to the peer review of this work.

Reprints and permissions information is available at www.nature.com/reprints.